Int. J. Heat Mass Transfer. Vol. 31, No. 6, pp. 1157–1165, 1988
Printed in Great Britain

0017–9310/88 $3.00+0.00

Heat transfer from an isothermal wedge in an air–water mist flow

W. S. FU and R. M. WU
Department of Mechanical Engineering, National Chiao Tung University, Hsinchu, Taiwan, 30049, R.O.C.

(*Received* 7 *May* 1987 *and in final form* 29 *September* 1987)

Abstract—An analysis has been made to investigate the influence of droplet trajectories and size distribution of polydisperse droplets on the heat transfer mechanism from an isothermal heated wedge put in air–water mist flow. To simplify the calculating process, an approximate calculation method with equivalent diameter theory is used. In the method, the equations of the water film flow have been solved by an integration method, while the equations of the gas flow have been solved by a finite difference method. The interface conditions between the water film and the gas layer have been determined by iterating the solutions of water and gas flows.

INTRODUCTION

ADDING water droplets into a single-phase gas flow which forms air–water mist flow can enhance the performance of heat transfer from the heated body. The main reason is that the heat transfer mechanism consists of not only the convection heat transfer of single-phase gas flow, but also the sensible heat transfer due to the temperature rise of the water film formed by the impingement of cold droplets on the heated body, and the evaporation heat transfer from the water film. The enhancement of the heat transfer coefficient may contribute a significant reduction in the size of a heat exchanger and can also be used for the emergency cooling system in a nuclear reactor.

In the past, Hishida *et al.* [1], and Trela [2] analysed heat transfer from a flat plate in air–water mist flow. References [3–5] investigated heat transfer in an air–water mist flow over an isothermal wedge experimentally and theoretically. In order to simplify the theoretical analysis, the trajectories were assumed to be straight lines and congruent with the far-upstream gas-phase velocity. Goldstein *et al.* [6], and Hodgson and Sunderland [7] investigated heat transfer in air–water mist flow over an isothermal cylinder. The former considered the influence of the trajectories of droplets without assuming them to be straight lines and neglected the effect of evaporation, while the latter considered the droplet trajectories to be straight lines and also neglected the evaporation effect. Nishikawa and Takase [8], and Lu and Heyt [9] investigated heat transfer in air–water mist flow over an isothermal cylinder, taking into account evaporation in the analyses. The former assumed the droplet trajectories to be congruent with the gas-phase streamlines; the latter considered the influence of the droplet trajectories which were not assumed to be straight. In all the theoretical analyses mentioned above, the droplets were considered to be uniform, which means the droplets are monodisperse.

Besides the influence of droplet trajectories, ref. [10] also considered the influence of the droplet size distribution of polydisperse droplets on heat transfer in water–mist flow over an isothermal cylinder. Due to the consideration of both the droplet trajectories and size distribution, the process of calculating the heat transfer coefficient became very complicated. In order to simplify the process, ref. [11] proposed two methods using the equivalent diameter theory and the Lewis relation, and the results were positive.

The goal of this study is to use the equivalent diameter theory to study the influence of droplet trajectories and size distribution of polydisperse droplets on heat transfer in air–water mist flow over an isothermal wedge. The results of numerical calculations are compared with the experimental results of Thomas and Sunderland [3] to illustrate the validity of the theoretical analysis. In the analysis, the authors rely on the related data obtained by Tsay [12] for both the droplet trajectories over the wedge and the variations of the size distribution before and after the droplets impinge on the wedge.

PHYSICAL MODEL

The physical model of air–water mist flow over an isothermal wedge is shown in Fig. 1. An isothermal wedge with an upward apex angle is laid horizontally in an air–water mist flow. The length of the wedge surface is L, the apex angle is β, the temperature of the mainstream humid air is T_∞ and the relative humidity is $\phi_\infty = 100\%$ and the droplet temperature is T_d. The upstream droplets impinge on the wall surface or water film with impinging velocities V_{pi} and impinging angle α. Because of a higher wall temperature, the droplets absorb heat energy after impinging on the heated body which causes both the sensible heat transfer and the evaporation heat transfer to occur respectively in the water film. If the impinging

NOMENCLATURE

C_p specific heat [J kg^{-1}K^{-1}]
d_e absolute size constant of Rosin–Rammler size distribution [m]
d_p droplet diameter [m]
D binary diffusion coefficient [m^{2}s^{-1}]
$f_{w(d)}$ mass-basis size distribution function of Rosin–Rammler size distribution
g gravitational acceleration, 9.8 m s^{-2}
G_e mass evaporation rate of water film [kg m^{-2}s^{-1}]
$G_{g\infty}$ mass flow rate of humid air [kg m^{-2}s^{-1}]
$G_{pi(d,x)}$ partial impinging mass flow rate for droplet size d [kg m^{-2}s^{-1}]
$G_{pi(x)}$ total impinging mass flow rate for droplets [kg m^{-2}s^{-1}]
$G_{p\infty}$ mass flow rate far upstream for droplets [kg m^{-2}s^{-1}]
$G_{p\infty(d)}$ mass flow rate far upstream for droplet size d [kg m^{-2}s^{-1}]
h heat transfer coefficient [W m^{-2}K^{-1}]
H absolute humidity
L length of a wedge surface [m]
M mass flow ratio, $G_{p\infty}/G_{g\infty}$
N_e distribution size of Rosin–Rammler size distribution
Nu Nusselt number
Pr Prandtl number
$\dot{q}$ heat flux on wedge surface [W m^{-2}]
r latent heat of evaporation [J kg^{-1}]
Sc Schmidt number
$T, \Delta T_w$ temperature and temperature difference, $T_w - T_\infty$ [K]
T_d droplet temperature [K]
u, v velocities in the x- and y-directions [m s^{-1}]
u_e velocity at edge of gas-phase boundary layer [m s^{-1}]
$V_{pi(d,x)}$ impinging velocity for droplet size d [m s^{-1}]
x, y Cartesian coordinates
x_0 starting point of water film [m].

Greek symbols
α impinging angle [rad]
β apex angle of a wedge [rad]
δ thickness of gas-phase boundary layer [m]
δ_l thickness of water film [m]
$\eta_{(d,x)}$ local partial impingement efficiency for droplet size d
$\eta_{(x)}$ local total impingement efficiency for droplets
λ thermal conductivity [W m^{-1}K^{-1}]
μ viscosity [Pa s]
ν kinetic viscosity [m^{2}s^{-1}]
ρ density [kg m^{-3}]
τ shear stress [N m^{-2}]
ω mass concentration of humid air, $H/(1+H)$.

Subscripts
d droplet diameter
d_e equivalent diameter
g gas phase (humid air)
i gas–water film interface
j, k grid indices in the X- and Y-directions
l water film
w wedge surface
∞ far upstream
(1) gas-phase (humid air) film
(2) air–water mist flow.

mass flow rate of droplets is smaller than the mass evaporation rate on the heated surface, no droplets remain on the heated surface, and thus a dryout region ($0 < x < x_0$) is formed. On the contrary, if the impinging mass flow rate of droplets is greater than the mass evaporation rate on the heated surface, a water film will be formed on the surface (a wet region $x_0 < x$).

In order to simplify the analysis, the following assumptions are made.

(1) Air–water mist flow is a two-dimensional and incompressible fluid, while the water film layer and the gas-phase layer are both laminar flows.

(2) Droplets are solid spheres, in which the motion of every droplet is regarded as a single solid sphere motion. In addition, no evaporation, impingement or combination occurs during the movement.

(3) For making the physical model close to the actual condition, water droplets far upstream have a mass-basis Rosin–Rammler size distribution and are uniformly distributed.

(4) The gas-phase boundary layer is not influenced by the passing of droplets.

(5) No re-entrainment occurs. Moreover, the effect of surface tension is not considered in the analysis.

(6) As the mass flow ratio is relatively small and as the water film is also very thin, water film velocity and temperature have a linear distribution. On impinging upon the wedge surface, the droplets immediately heat up to the temperature of the gas–water film interface.

(7) The properties are based on referential temperature $T_r = (T_w + T_\infty)/2$ and referential concentration $\omega_r = (\omega_w + \omega_\infty)/2$.

(8) The condition at the wall surface or gas–water film interface is in saturation.

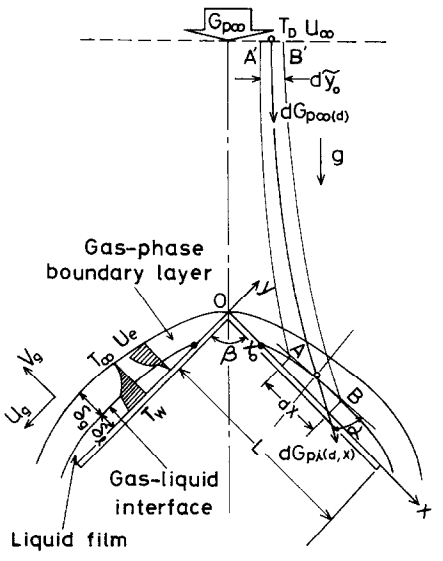

FIG. 1. Physical model.

The dryout region governing equation

The heat transfer near the tip of the wedge is relatively large, the impinging mass flow rate is smaller than the mass evaporation rate; meanwhile, all the droplets evaporated so that no water film could be formed, thus becoming the dryout region. Therefore, the water film thickness and wall temperature at the leading edge ($x = 0$) are 0 and T_w, respectively; the boundary layers of the gas-phase flow begin to grow there. As X increases along with the wedge surface, the heat transfer decreases and thus causes the mass evaporation rate to decrease. Therefore, a point x_0 where the mass evaporation rate is equivalent to the impinging mass flow rate may be determined, the water film starts to form beyond this point.

So in the range of $0 < x < x_0$, the wall surface is covered only by a gas-phase layer, the governing equations of which are

$$\frac{\partial u_g}{\partial x} + \frac{\partial v_g}{\partial y} = 0 \tag{1a}$$

$$u_g \frac{\partial u_g}{\partial x} + v_g \frac{\partial u_g}{\partial y} = u_e \frac{\partial u_e}{\partial x} + \nu_g \frac{\partial^2 u_g}{\partial y^2} \tag{1b}$$

$$u_g \frac{\partial T_g}{\partial x} + v_g \frac{\partial T_g}{\partial y} = \frac{\lambda_g}{C_{pg}\rho_g} \frac{\partial^2 T_g}{\partial y^2} \tag{1c}$$

$$u_g \frac{\partial \omega_g}{\partial x} + v_g \frac{\partial \omega_g}{\partial y} = D_g \frac{\partial^2 \omega_g}{\partial y^2}. \tag{1d}$$

Because the droplets impinge on the wall surface and are completely evaporated, the boundary conditions are obtained as

$$\left.\begin{aligned} &y = 0, \quad u_g = 0, \quad v_{gi} = G_{pi(x)}/\rho_g \\ &T_g = T_w, \quad \omega_g = \omega_w, \quad y \to \infty \\ &u_g = u_e, \quad T_g = T_\infty, \quad \omega_g = \omega_\infty \end{aligned}\right\} \tag{2}$$

with

$$G_{pi(x)} = G_{p\infty}\eta(x).$$

The wet region governing equation

As mentioned above, when $x_0 < x$ the water film starts to form, there is a water film layer on the wedge wall, with a gas-phase layer formed above the water film layer. The governing equations of the water film and the gas phase are given below.

The gas-phase layer equations. The governing equations of the gas-phase layer are identical to equation (1) of the dryout region, but boundary conditions are different and can be written as

$$\left.\begin{aligned} &y = \delta_l, \quad u_g = u_i, \quad T_g = T_i \\ &\omega_g = \omega_i, \quad v_{gi} = G_e/\rho_g \\ &y \to \infty, \quad u_g = u_e, \quad T_g = T_\infty, \quad \omega_g = \omega_\infty \end{aligned}\right\} \tag{3}$$

with

$$G_e = \frac{-\rho_g D_g}{1-(\omega_g)_i}\left(\frac{\partial \omega_g}{\partial y}\right)_i. \tag{4}$$

The water film equations. From ref. [5], the acceleration and convection terms in the momentum and energy equations can be neglected. Refer to ref. [10], the continuity momentum and energy equations of the water film can be expressed separately as

$$G_{p\infty}\eta_{(x)}\,dx - \rho_l \frac{\partial}{\partial x}\left(\int_0^{\delta_l} u_l\,dy\right)dx = G_e\,dx \tag{5}$$

$$\tau_w\,dx = -\delta_l \frac{dp}{dx}dx + \rho_l \delta_l g \cos\left(\frac{\beta}{2}\right)dx + \tau_{gi}\,dx + \left[\int_{(d_p)_{min}}^{(d_p)_{max}} \left[\sin\alpha + \cos\alpha\left(\frac{d\delta_l}{dx_l}\right)\right]\cdot v_{pi(d,x)} \cdot \cos\alpha_{(d,x)}\,dG_{pi(d,x)}\right]dx. \tag{6}$$

In equation (6), the left-hand side is the shear force on the wedge wall and the four terms on the right-hand side are pressure force, gravity force, gas–liquid shear force and droplet impinging force. In equation (6), $V_{pi(d,x)}$ means that the d size droplet with velocity V impinges at position x on the wedge. The direction of it is the same as $dG_{pi(d,x)}$ shown in Fig. 1. Reference [13] defines $\eta_{(d,x)}$ as the impingement efficiency of d size droplet at position x

$$\dot{q}_w\,dx = h_g(T_i - T_\infty)\,dx + G_e r_i\,dx + G_{p\infty}\eta_{(x)}C_{pl}(T_i - T_d)\,dx. \tag{7}$$

In equation (7), the term on the left-hand side is the heat flux on the wedge wall and the three terms on the right-hand side are the convection heat transfer of the gas-phase flow, evaporation heat transfer and sensible heat transfer of droplet impingement.

The local total impingement efficiency $\eta_{(x)}$ is obtained from Tsay [12] and defined as

$$\eta_{(x)} = \int_{(d_p)_{min}}^{(d_p)_{max}} \eta_{(d,x)} f_{w(d)}\, d(d_p). \quad (8)$$

The values of impinging velocity $V_{pi(d,x)}$, impinging angle $\alpha_{(d,x)}$ and local partial impingement efficiency $\eta_{(d,x)}$ were also obtained by Tsay [12].

SOLUTION METHODOLOGY

For the convenience of the analysis, the following dimensionless variables are used:

$$\left.\begin{aligned} U &= \frac{u}{u_e}, \quad V = \frac{v}{u_e}\sqrt{\left(\frac{u_\infty L}{\nu_g}\frac{1+m}{2}\right)}, \quad \theta = \frac{T-T_\infty}{T_w-T_\infty} \\ X &= \frac{x}{L}, \quad Y = \frac{y}{L}\sqrt{\left(\frac{u_\infty L}{\nu_g}\frac{1+m}{2}\right)}, \quad W = \frac{\omega-\omega_\infty}{\omega_w-\omega_\infty} \\ \delta_l^+ &= \frac{\delta_l}{L}, \quad U_e = \frac{u_e}{u_\infty}, \qquad\qquad M = \frac{G_{p\infty}}{G_{g\infty}} \end{aligned}\right\} \quad (9)$$

u_e obtained by Tsay [12].

The numerical solution adopts the finite difference method in this study which is the same as in ref. [10]. In the X-direction the backward finite difference method is used; in the Y-direction the central difference method is used; while non-linear coefficients are approximately substituted by convergence values in the proceeding iteration.

The dryout region governing equations

By using the dimensionless variables and finite difference methods, equation (1) becomes

$$\frac{1}{U_{e(j)}}\frac{U_{e(j)}U_{(j,k)} + U_{e(j)}U_{(j,k-1)} - U_{e(j-1)}U_{(j-1,k)} - U_{e(j-1)}U_{(j-1,k-1)}}{2\Delta X} + \frac{V_{(j,k)} - V_{(j,k-1)}}{\Delta Y} = 0 \quad (10a)$$

$$\frac{U^*_{(j,k)}}{U_{e(j)}}\frac{U_{e(j)}U_{(j,k)} - U_{e(j-1)}U_{(j-1,k)}}{\Delta X} + V^*_{(j,k)}\frac{U_{(j,k+1)} - U_{(j,k-1)}}{2\Delta Y} = \frac{1}{U_{e(j)}}\frac{U_{e(j)} - U_{e(j-1)}}{\Delta X} + \frac{1}{U_{e(j)}}\frac{1+m}{2}\frac{U_{(j,k+1)} - 2U_{(j,k)} + U_{(j,k-1)}}{\Delta Y^2} \quad (10b)$$

$$U_{(j,k)}\frac{\theta_{(j,k)} - \theta_{(j-1,k)}}{\Delta X} + V_{(j,k)}\frac{\theta_{(j,k+1)} - \theta_{(j,k-1)}}{2\Delta Y} = \frac{1}{U_{e(j)}}\frac{1+m}{2}\frac{1}{Pr}\frac{\theta_{(j,k+1)} - 2\theta_{(j,k)} + \theta_{(j,k-1)}}{\Delta Y^2} \quad (10c)$$

$$U_{(j,k)}\frac{W_{(j,k)} - W_{(j-1,k)}}{\Delta X} + V_{(j,k)}\frac{W_{(j,k+1)} - W_{(j,k-1)}}{2\Delta Y} = \frac{1}{U_{e(j)}}\frac{1+m}{2}\frac{1}{Sc}\frac{W_{(j,k+1)} - 2W_{(j,k)} + W_{(j,k-1)}}{\Delta Y^2}. \quad (10d)$$

Subscript * denotes the value of the preceding iteration. The boundary conditions are

$$\left.\begin{aligned} &Y = 0, \ U = 0, \ V_{gi} = \frac{G_{pi(x)}}{\rho_{g\infty}U_e}\sqrt{\left(\frac{u_\infty L}{\nu_g}\frac{1+m}{2}\right)} \\ &\theta = 1, \ W = 1 \\ &Y \to \infty, \ U = 1, \ \theta = 0, \ W = 0. \end{aligned}\right\} \quad (11)$$

The wet region governing equations

The governing equations of water film. Because the water film is very thin, the velocity and temperature distributions can be assumed as

$$u_l = \left(\frac{y}{\delta_l}\right)u_i \quad (12)$$

$$T_l = T_w - \left(\frac{y}{\delta_l}\right)(T_w - T_i). \quad (13)$$

Substitution of equations (12) and (13) into governing equations (5)–(7) of the water film give

$$M\eta_{(x)}\frac{\rho_g}{\rho_l}\frac{1}{u_\infty U_{e(j)}} - \frac{1}{2}\frac{1}{U_{e(j)}u_\infty} \times \frac{\delta^+_{l(j)}U_{e(j)}U_{i(j)} - \delta^+_{l(j-1)}U_{e(j-1)}U_{i(j-1)}}{\Delta X} = G_e/(\rho_l U_{e(j)}u^2_\infty) \quad (14)$$

with

$$M = G_{p\infty}/G_{g\infty}, \quad G_{g\infty} = \rho_g u_\infty$$

$$\frac{\mu_{lw}U_{i(j)}}{L\delta^+_{l(j)}u_\infty U_{e(j)}\rho_l} = \frac{\rho_g\delta^{+*}_{l(j)}}{\rho_l U_{e(j)}}\frac{U_{e(j)} - U_{e(j-1)}}{\Delta X} + \frac{gL\delta^{+*}_{l(j)}\cos(\beta/2)}{u^2_\infty U^2_{e(j)}} + \frac{\mu_{gl}}{L\rho_l u_\infty U_{e(j)}} \times \sqrt{\left(\frac{u_\infty L}{\nu_g}\frac{1+m}{2}\right)}\left(\frac{\partial U}{\partial Y}\right)^*_{i(j)} + G_{p\infty}\int_{(d_p)_{min}}^{(d_p)_{max}} \eta_{(d,x)}f_{w(d)}\cdot v_{pi(d,x)} \cdot \cos\alpha_{(d,x)}\cdot d(d_p)/(\rho_l u^2_\infty U^2_{e(j)}) \quad (15)$$

$$\frac{\lambda_{lw}(1-\theta_{i(j)})}{L\delta^+_{l(j)}} = -\lambda_{gi}\left(\frac{\partial\theta}{\partial Y}\right)^*_{i(j)}\frac{1}{L}\sqrt{\left(\frac{u_\infty L}{\nu_g}\frac{1+m}{2}\right)} + \frac{G_e r^*_{i(j)}}{T_w - T_\infty} + G_{p\infty}\eta_{(x)}C_{pl}\left(\theta^*_{i(j)} + \frac{T_\infty - T_d}{T_w - T_\infty}\right). \quad (16)$$

The gas-phase governing equations. The governing equations of the gas phase are identical to those of the dryout region. The boundary conditions are

$$\left.\begin{aligned} &Y=\sqrt{\left(\frac{u_\infty L}{\nu_g}\frac{1+m}{2}\right)}\delta_i^+\\ &U_g=U_i,\quad \theta_g=\theta_i,\quad W_g=W_i\\ &V_{gi}=\frac{G_e}{\rho_g u_\infty U_e}\sqrt{\left(\frac{u_\infty L}{\nu_g}\frac{1+m}{2}\right)}\\ &Y\to\infty,\quad U_g=1,\quad \theta_g=0,\quad W_g=0. \end{aligned}\right\} \quad (17)$$

The equivalent diameter approximate calculation method

During the analysis of air–water mist flow heat transfer, the trajectories and size distribution of polydisperse droplets are correlated with the results, shown in terms of the local partial impingement efficiency $\eta_{(d,x)}$, the impinging velocity $V_{pi(d,x)}$, the impinging angle $\alpha_{(d,x)}$ and the size distribution function $f_{w(d)}$ [10]. In order to obtain the exact solutions, the foregoing related numerical values of every droplet diameter have to be calculated; thus, the calculation process is extremely complicated. To simplify the analytical process, the present study has adopted the approximate calculation method with the equivalent diameter theory taken from ref. [11], in which the equivalent diameter [13] represents polydisperse droplets, and thus immensely simplify the numerical calculation process. Accordingly, in equations (14) and (16), $\eta_{(x)}$ is replaced by $\eta_{(d_e,x)}$. In equation (15)

$$\int_{(d_p)_{min}}^{(d_p)_{max}}\eta_{(d,x)}f_{w(d)}|V_{pi(d,x)}|\cos\alpha_{(d,x)}\,d(d_p)$$

is replaced by

$$\eta_{(d_e,x)}\cdot V_{pi(d_e,x)}\cdot\cos\alpha_{(d_e,x)}.$$

Through these substitutions, the calculation process can thus be simplified, but the accuracy of the calculations is not affected.

The numerical methodology of the dryout region

Boundary conditions (11) in the dryout region are substituted into governing equations (10), and momentum, energy and concentration equations can be formed into tri-diagonal matrix equations. First, the velocity distribution U is derived from the momentum equation; also, from the continuity equation the velocity V is derived, which is substituted into the energy equation. Then, the temperature distribution θ is obtained; finally from the concentration equation the concentration distribution ω is derived. While using this method, the thickness of the gas-phase layer is indispensable and is approximated by the result of Eckert and Drake [14]

$$\delta=\sqrt{\left(\frac{2}{m+1}\frac{vx}{u_e}\right)}\eta_\delta \quad (18)$$

where η_δ is the similarity transform variable.

The convergent condition of the iteration calculation is

$$|[U^*_{(j,k)}-U_{(j,k)}]/U_{(j,k)}|<10^{-3} \quad (19)$$

where superscript * denotes the value of the preceding iteration.

The solution methodology of the wet region

The water film starts to form at $G_{e(x)}=G_{pi(x)}$. The point where the water film starts forming is x_0 and the grid index is j_0. The conditions of the water film are assumed as

$$\delta^+_{i(j0)}=0,\quad U_{i(j0)}=0,\quad \theta_{i(j0)}=1. \quad (20)$$

The solution method of the gas phase is identical with that of the dryout region. The momentum equation (15) of the water film can be written as

$$U_{i(j)}=\delta^+_{i(j)}\cdot R_1 \quad (21)$$

where

$$R_1=\frac{Lu_\infty U_{e(j)}\rho_l}{\mu_{tw}}\left[\frac{\rho_g}{\rho_l}\frac{\delta^{+*}_{i(j)}}{U_{e(j)}}\frac{U_{e(j)}-U_{e(j-1)}}{\Delta X}+\frac{gL\delta^{+*}_{i(j)}\cos(\beta/2)}{u_\infty^2U^2_{e(j)}}+\frac{\mu_{gi}}{L\rho_l u_\infty U_{e(j)}}\times\sqrt{\left(\frac{u_\infty L}{\nu_g}\frac{1+m}{2}\right)}\left(\frac{\partial U}{\partial Y}\right)^*_{i(j)}+G_{p\infty}\eta_{(d_e,x)}|v_{pi(d_e,x)}|\cos\alpha_{(d_e,x)}/\rho_l u_\infty^2U^2_{e(j)}\right]. \quad (22)$$

Substituting equation (22) into continuity equation (14) and rearranging gives

$$\delta^+_{i(j)}=\sqrt{(R_2/R_1)} \quad (23)$$

where

$$R_2=2u_\infty\Delta X\left[M\eta_{(d_e,x)}\frac{\rho_g}{\rho_l}\frac{1}{u_\infty U_{e(j)}}+\frac{\delta^+_{i(j-1)}U_{i(j-1)}}{2u_\infty\Delta X}\frac{U_{e(j-1)}}{U_{e(j)}}-G_e/\rho_l U_{e(j)}u_\infty^2\right]. \quad (24)$$

Thus the energy equation can be written as

$$\theta_{i(j)}=1-\frac{L\delta^+_{i(j)}}{\lambda_{tw}}\left[-\lambda_{gi}\left(\frac{\partial\theta}{\partial Y}\right)^*_{i(j)}\times\frac{1}{L}\sqrt{\left(\frac{u_\infty L}{\nu_x}\frac{1+m}{2}\right)}+\frac{G_e r^*_{i(j)}}{T_w-T_\infty}+G_{p\infty}\eta_{(d_e,x)}C_{pl}\left(\theta^*_{i(j)}+\frac{T_\infty-T_d}{T_w-T_\infty}\right)\right]. \quad (25)$$

During the simultaneous calculating water film and gas-phase equations process, when the water film equation is calculated once, the gas-phase equations are iteratively calculated till they are convergent. When the following convergence conditions are all satisfied, the calculation process of this step j is accomplished and the next step is started. Convergent

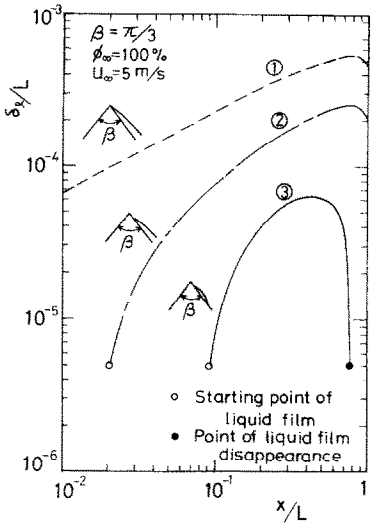

FIG. 2. The shapes of a water film on a heated surface: (1) $M = 5 \times 10^{-3}$, $\Delta T_w = 30$ K, $N_c = 3$, $d_c/L = 2 \times 10^{-3}$; (2) $M = 1 \times 10^{-3}$, $\Delta T_w = 20$ K, $N_c = 3$, $d_c/L = 2 \times 10^{-3}$; (3) $M = 1 \times 10^{-3}$, $\Delta T_w = 22$ K, $N_c = 4$, $d_c/L = 1 \times 10^{-3}$.

values of the jth step are used as initial values of the $(j+1)$th step if necessary

$$\left.\begin{aligned} &|(\delta^{+*}_{i(j)} - \delta^{+}_{i(j)})/\delta^{+}_{i(j)}| < 10^{-3} \\ &|(U^{*}_{i(j)} - U_{i(j)})/U_{i(j)}| < 10^{-3} \\ &|(\theta^{*}_{i(j)} - \theta_{i(j)})/\theta_{i(j)}| < 10^{-3} \\ &|[U^{*}_{(j,k)} - U_{(j,k)}]/U_{(j,k)}| < 10^{-3}. \end{aligned}\right\} \quad (26)$$

RESULTS AND DISCUSSION

In this study, the wedge length L is 0.05 m and the mainstream temperature T_∞ is 285.15 K. The relative humidity of the mainstream is 100%.

Due to the influence on the water film formed over the heated body in an air–water mist flow from various factors, the water film may have different shapes, as shown in Fig. 2. During the calculation, if the thickness of the water film δ_i^+ is less than 5×10^{-6}, the water film is regarded as nonexistent. Curve 1 shows that the wall surface is completely covered by the water film. When the mass flow ratio M is large; in this condition, the impinging mass flow rate is always larger than the mass evaporation rate on the whole wall surface. Curve 2 shows that the upper section dries out, while the lower section is covered by the water film which happens when the mass flow ratio M is not very large. The mass evaporation rate is greater than the impinging mass flow rate in the upper section and smaller than it in the lower section. Curve 3 shows that the upper and lower sections dry out while it is wet in the middle. If both the size of droplets and the mass flow rate are small, this kind of water film can be formed. Small droplets in the air–water flow, which travel more easily circuitously over the wedge [12], causes the impinging mass flow rate to decrease drastically and become far smaller than the mass evaporation rate in the lower section. So the dryout region occurs again.

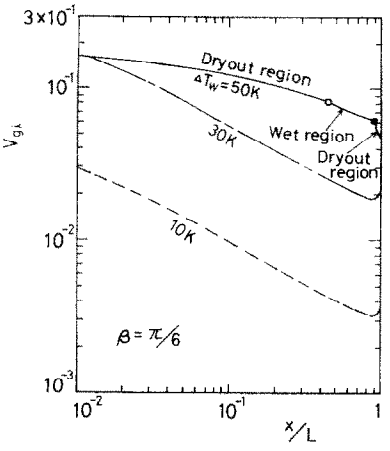

FIG. 3. Influence of the temperature difference ΔT_w on evaporation velocity V_{gi} ($u_\infty = 5$ m s^{-1}, $M = 5 \times 10^{-3}$, $N_c = 3$, $d_c/L = 2 \times 10^{-3}$).

Figure 3 shows the influence of temperature differences ΔT_w on the evaporation velocity V_{gi}. From the plot the result that while X increases, V_{gi} decreases can be derived. Furthermore, the water film becomes thicker, and the interface temperature T_i becomes smaller which consequently decreases the evaporation performance. However, in the lower section, due to the flow acceleration, as the water film becomes thinner, evaporation thus increases. When the temperature difference ΔT_w is greater, the evaporation velocity also increases. As in Fig. 3, when $\Delta T_w = 50$ K, the condition of the wall surface changes from the dryout region to the wet region and then to the dryout region. Within the wet region where the water film exists, the interface temperature T_i is less than the wall surface temperature T_w, and thus V_{gi} becomes smaller. In the downstream dryout region, a discontinuous phenomenon occurs. The reason is that in the latter part of the wet region, the mass evaporation rate is gradually greater than the impinging mass flow rate and part of the water film begins to evaporate. Therefore, the water film decreases little by little, when the water film disappears, there is only the impinging mass flow rate left to be evaporated, which suddenly decreases the evaporation velocity and forms a discontinuous phenomenon.

Figure 4 shows the influence of mass flow ratio M on the Nusselt number. Nusselt number $Nu_{(2)}$ is defined as

$$\left.\begin{aligned} Nu_{(2)} &= h_{(2)} X/(\lambda_l)_w \\ h_{(2)} &= \dot{q}_w/\Delta T_w \end{aligned}\right\} \quad (27)$$

where $\dot{q}_w$ is derived from equation (7).

The greater the mass flow ratio, the larger the impinging mass flow rate becomes, and the Nusselt number $Nu_{(2)}$ increases.

The greater the temperature difference ΔT_w, as shown in Fig. 5, the greater the Nusselt number $Nu_{(2)}$ becomes. The changes of the heated surface are from the dryout region to the wet region and then to the

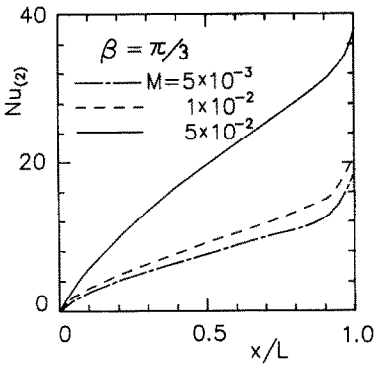

FIG. 4. Influence of mass flow ratio M on the Nusselt number $Nu_{(2)}$ ($u_\infty = 5$ m s^{-1}, $\Delta T_w = 30$ K, $N_c = 3$, $d_c/L = 2 \times 10^{-3}$).

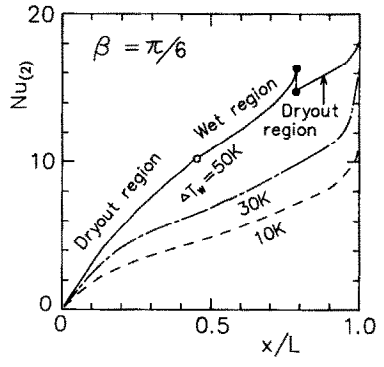

FIG. 5. Influence of the temperature difference ΔT_w on the Nusselt number $Nu_{(2)}$ ($u_\infty = 5$ m s^{-1}, $M = 5 \times 10^{-3}$, $N_c = 3$, $d_c/L = 2 \times 10^{-3}$).

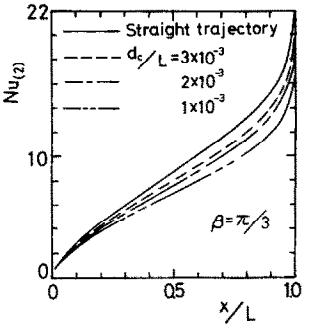

FIG. 6. Influence of absolute size constant d_c on the Nusselt number $Nu_{(2)}$ ($u_\infty = 5$ m s^{-1}, $\Delta T_w = 30$ K, $M = 5 \times 10^{-3}$, $N_c = 3$).

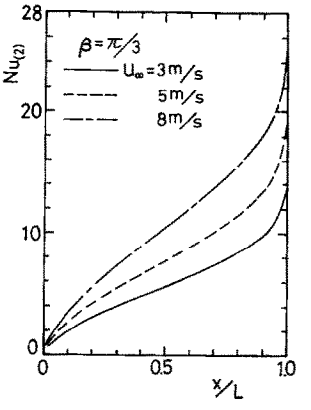

FIG. 7. Influence of the far-upstream velocity U_∞ on the Nusselt number $Nu_{(2)}$ ($M = 5 \times 10^{-3}$, $\Delta T_w = 30$ K, $N_c = 3$, $d_c/L = 2 \times 10^{-3}$).

dryout region with $\Delta T_w = 50$ K. When the region is changed from wet to dryout, the quantity of evaporated mass decreases suddenly which causes the Nusselt number to decrease drastically, the reason is similar to that described above. When adopting a water mist flow to cool the heated body, this situation should be avoided.

The influence of absolute size constant d_c on Nusselt number $Nu_{(2)}$ is shown in Fig. 6. When the value of d_c is small, it indicates that there are plenty of smaller diameter droplets in a mist flow; the impingement efficiencies of smaller droplets are smaller which make $Nu_{(2)}$ also smaller. When the trajectory is to be in straight lines the impingement efficiency of droplets is larger, therefore $Nu_{(2)}$ is greater; however, consideration of the size distribution of polydisperse droplets is meaningless at this condition.

Usually when the mainstream velocity u_∞ is high, the impinging mass flow rate of droplets also increases, as shown in Fig. 7, and $Nu_{(2)}$ also increases. The contribution of the sensible heat transfer increases with the increase of impinging mass flow rate. Moreover, the mainstream velocity also influences the gas-phase convection heat transfer, but the contribution is smaller than the former one.

The heat transfer enhancement rate F_e is defined by

$$F_e = h_{(2)}/h_{(1)} \tag{28}$$

where $h_{(2)}$ and $h_{(1)}$ are the heat transfer coefficients of the heated surface in an air–water mist flow and a single gas-phase flow, respectively. From Tsay [12], the greater the angle, the better the impinging effect of droplets becomes and thus F_e increases, as shown in Fig. 8. As position X increases, F_e also increases, but it decreases within the extremely low section of the wedge.

Figure 9 shows the comparison between the numerical solutions in this study with the results of Thomas and Sunderland's experiment [3]. The apex angle of the wedge in ref. [3] is $\pi/9$ rad. In order to compare the

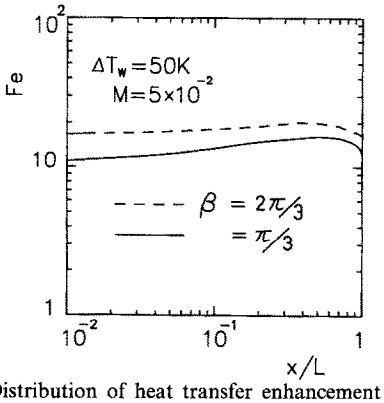

FIG. 8. Distribution of heat transfer enhancement rate F_e ($u_\infty = 5$ m s^{-1}, $N_c = 3$, $d_c/L = 2 \times 10^{-3}$).

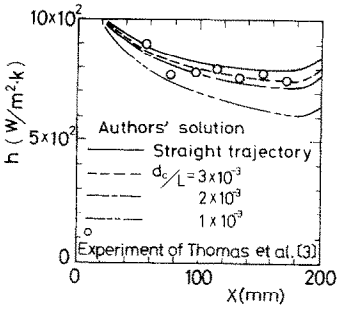

FIG. 9. Comparison of the numerical solution of the present study with the experimental results of Thomas and Sunderland [3] ($\beta = \pi/9$, $M = 0.057$, $u_\infty = 15.1$ m s^{-1}, $T_w = 313.75$ K, $T_\infty = 302.55$ K, $N_c = 3$).

results, the calculation of the heat transfer coefficient h is performed by extrapolating the results of $\pi/6$, $\pi/3$, $\pi/2$, $2\pi/3$ rad into $\pi/9$ rad in the present study. As the droplet size distribution in Thomas and Sunderland's experiment is unknown, a quantitative comparison cannot be operated. Therefore, calculation of the possible size distribution [4] is taken to have a qualitative comparison with the experimental value. From the figure, one can see that the experimental value agrees better with the larger d_c value. The reason is likely to be that the experiment of Thomas and Sunderland was done by placing the wedge in the wind tunnel. Due to the influence of the wall surface blockage effect [15], the impingement efficiency will be greater. Thus when comparing the results of Thomas and Sunderland's experiment with that of this study, their results correlate better with the larger d_c value of the present study.

CONCLUSIONS

The problem of heat transfer from an isothermal wedge in air–water mist flow was investigated. Droplets with the Rosin–Rammler size distribution were taken into consideration. An equivalent diameter theory was adopted in the theoretical analysis. The following results were obtained.

(1) An equivalent diameter theory is effective in analysing the problem of the heat transfer of a heated wedge in an air–water mist flow.

(2) To make the physical model close to the actual situation, the consideration of droplets suspended in air–water mist flow with size distribution and nonlinear trajectories is necessary.

(3) Large values of the absolute size constant increase the Nusselt number.

Acknowledgements—The financial support of this study by the Engineering Division, National Research Council of Taiwan, R.O.C., is greatly appreciated. The authors also wish to express their gratitude to Dr Lin, Mr Yang, Mr Peng and Ms Hsieh for their assistance.

REFERENCES

1. K. Hishida, M. Maeda and S. Ikai, Heat transfer from a flat plate in two-component mist flow, *Trans. ASME J. Heat Transfer* **102**, 513–518 (1980).
2. M. Trela, An approximate calculation of heat transfer during flow of an air–water mist along a heated flat plate, *Int. J. Heat Mass Transfer* **24**, 749–755 (1981).
3. W. C. Thomas and J. E. Sunderland, Heat transfer between a plane surface and air containing suspended water droplet, *Ind. Engng Chem. Fundam.* **9**, 368–374 (1970).
4. T. Aihara, M. Taga and T. Haraguchi, Heat transfer from a uniform heat flux wedge in air–water mist flows, *Int. J. Heat Mass Transfer* **22**, 51–60 (1979).
5. T. Aihara and W. S. Fu, Heat transfer from a wedge in air–water mist flow, *Trans. Japan Soc. Mech. Engrs* (Ser. B) **48**, 2536–2546 (1982).
6. M. E. Goldstein, W. J. Yang and J. A. Clark, Momentum and heat transfer in laminar flow of gas with liquid-droplet suspension over a circular cylinder, *Trans. ASME J. Heat Transfer* **89**, 185–194 (1967).
7. J. W. Hodgson and J. E. Sunderland, Heat transfer from a spray-cooled isothermal cylinder, *Ind. Engng Chem. Fundam.* **7**, 567–572 (1968).
8. N. Nishikawa and H. Takase, Effect of particle size and temperature difference on mist flow over a heated circular cylinder, *Trans. ASME J. Heat Transfer* **11**, 705–711 (1979).
9. C. C. Lu and J. W. Heyt, Heat transfer from two-phase boundary layer on isothermal trajectory, *A.I.Ch.E. Jl* **26**, 762–769 (1980).
10. W. S. Fu and T. Aihara, Heat transfer from a heated body in air–water mist flow (3rd Report), *Trans. Japan Soc. Mech. Engrs* (Ser. B) **51**, 882–892 (1985).
11. W. S. Fu, Heat transfer from a heated cylinder in air water mist flow, Doctorial Thesis, Tohoku University, Sendai, Japan (1984).
12. G. J. Tsay, Theoretical study of trajectories of particles surrounding a wedge, Master's Thesis, National Chiao Tung University, Hsinchu, Taiwan, R.O.C. (1985).
13. T. Aihara and W. S. Fu, Effect of droplet-size distribution and gas-phase flow separation upon inertia collection of droplets by bluff-bodies in gas–liquid mist flow, *Int. J. Multiphase Flow* **12**, 389–403 (1986).
14. E. R. G. Eckert and R. M. Drake, Jr., *Analysis of Heat and Mass Transfer*, Chap. 7. McGraw-Hill, New York (1982).
15. W. S. Fu and T. Aihara, Heat transfer from a heated body in air–water mist flow (2nd Report), *Trans. Japan Soc. Mech. Engrs* (Ser. B) **51**, 874–881 (1985).

TRANSFERT THERMIQUE POUR UN DIEDRE ISOTHERME DANS UN ECOULEMENT AIR–BROUILLARD D'EAU

Résumé—On analyse l'influence des trajectoires des gouttelettes et de leur distribution en taille sur le mécanisme du transfert thermique à partir d'un dièdre chaud isotherme dans un écoulement air–brouillard d'eau. Pour simplifier les calculs, on utilise une méthode approchée avec une théorie du diamètre équivalent. Les équations de l'écoulement du film d'eau sont résolues par une méthode d'intégration, tandis que les équations de l'écoulement gazeux sont traitées par une méthode de différence finie. Les conditions d'interface entre film d'eau et couche de gaz sont déterminées par itération des solutions des deux écoulements d'eau et de gaz.

WÄRMEÜBERTRAGUNG AN EINER ISOTHERMEN KEILFÖRMIGEN OBERFLÄCHE IN EINER LUFT/WASSER-NEBELSTRÖMUNG

Zusammenfassung—Der Einfluß der Flugbahn und der Größenverteilung von polydispersen Wassertröpfchen auf den Wärmeübertragungs-Mechanismus an einer isothermen beheizten keilförmigen Oberfläche in einer Luft/Wasser-Nebelströmung wird untersucht. Zur Vereinfachung des Berechnungsverfahrens wird ein Näherungsalgorithmus auf der Basis der Theorie des "äquivalenten Durchmessers" verwendet. In dieser Methode werden die Gleichungen für die Wasserfilmströmung mit einem Integrationsverfahren gelöst, während die Gleichungen für die Gasströmung mit einem Finite-Differenzen-Verfahren gelöst werden. Die Grenzflächen-Bedingungen zwischen Wasserfilm und Gasschicht werden durch Iteration aus den Lösungen für die Strömung von Wasser und Gas bestimmt.

ТЕПЛООБМЕН ОТ ИЗОТЕРМИЧЕСКОГО КЛИНА В ПОТОКЕ ТУМАНА ВОЗДУХ-ВОДА

Аннотация—Анализируется влияние траекторий капель и распределения размеров полидисперсых капель на механизм теплообмена от изотермического нагретого клина, помощенного в поток воздуха с частичками воды. Для упрощения процесса счета используется метод эквиалентного диаметра. В указанном методе уравнения для потока пленки воды решаются интегральным методом, а уравнения потока газа—конечно-разностным. Условия на границе раздела пленка–газ определяется итерированием решений для потоков воды и газа.